PHYSICAL SCIENCE

Interlayer couplings, Moiré patterns, and 2D electronic superlattices in MoS_2/WSe_2 hetero-bilayers

Chendong Zhang,[1] Chih-Piao Chuu,[2] Xibiao Ren,[3] Ming-Yang Li,[4,5] Lain-Jong Li,[4,5] Chuanhong Jin,[3] Mei-Yin Chou,[2,6,7] Chih-Kang Shih[1]*

By using direct growth, we create a rotationally aligned MoS_2/WSe_2 hetero-bilayer as a designer van der Waals heterostructure. With rotational alignment, the lattice mismatch leads to a periodic variation of atomic registry between individual van der Waals layers, exhibiting a Moiré pattern with a well-defined periodicity. By combining scanning tunneling microscopy/spectroscopy, transmission electron microscopy, and first-principles calculations, we investigate interlayer coupling as a function of atomic registry. We quantitatively determine the influence of interlayer coupling on the electronic structure of the hetero-bilayer at different critical points. We show that the direct gap semiconductor concept is retained in the bilayer although the valence and conduction band edges are located at different layers. We further show that the local bandgap is periodically modulated in the *X*-*Y* direction with an amplitude of ~0.15 eV, leading to the formation of a two-dimensional electronic superlattice.

INTRODUCTION

Stacking two-dimensional (2D) atomic crystals with different bandgaps into van der Waals (vdW) heterostructures has emerged as a very powerful method to create designer heterostructures (*1*). In designing these vdW heterostructures, the effect of interlayer coupling will play a critical role. As shown in graphene–hexagonal boron nitride (hBN) heterostructures, interlayer coupling can be tuned through spatial alignments between vdW layers, providing a designing parameter (without a counterpart in conventional heterostructures) to tailor the electronic structures of vdW heterostructures (*2*–*8*). The emergence of transition metal dichalcogenide (TMD)–based heterostructures brought again the role of interlayer coupling into the spotlight (*9*–*12*). The issue of interlayer coupling in TMD heterostructures is inherently complex. It is already known that for bilayer TMDs (referred to as homo-bilayers), interlayer coupling splits the degeneracy at the Γ point and transforms the direct gap in the monolayer (ML) into an indirect gap semiconductor (*13*, *14*). This splitting is shown to be quite large (~0.7 eV) (*14*–*16*). It has also been seen that the rotational alignment can influence the interlayer coupling in these homo-bilayers although all exhibit an indirect bandgap (*17*–*20*). For heterostructures composed of two different ML-TMD materials (referred to as hetero-bilayers), the role of interlayer coupling remains an open issue (*9*–*12*, *21*–*25*). Two questions stand out prominently: (i) Does interlayer coupling lead to an indirect gap in the hetero-bilayer, or is the direct gap retained? (ii) Can interlayer coupling be used as a design parameter for vdW TMD heterostructures?

Here, we examine these critical issues by using a rotationally aligned, lattice-mismatched MoS_2/WSe_2 heterostructure. Even with rotational alignment, the lattice mismatch between the two atomic layers produces a periodic variation in the lateral atomic registry, facilitating a natural platform for the investigation of how lateral registry affects interlayer coupling. The structural information is directly probed using scanning tunneling microscopy (STM) and transmission electron microscopy (TEM). Direct correlation of the lateral registry between the two atomic layers and the local electronic structures is revealed using comprehensive scanning tunneling spectroscopy (STS). Experimental observations are corroborated with first-principles calculations. We quantitatively show how interlayer coupling affects the electronic structure at different critical points. We find that the direct gap is retained with the valence and conduction band edges located at the same *K* point but in different layers. The local bandgap is modulated periodically in the *X*-*Y* direction with an amplitude of ~0.15 eV, creating an electronic superlattice.

RESULTS AND DISCUSSION

Chemical vapor deposition (CVD) is used to achieve direct growth of vertically stacked ML-MoS_2 on ML-WSe_2 on graphite substrates (described in Materials and Methods) (*26*). Figure 1A is an STM image of this hetero-bilayer on a graphite substrate. The Moiré pattern with a lattice constant of 8.7 ± 0.2 nm can be clearly observed on the top MoS_2 layer (zoom-in view shown in Fig. 1B). This superlattice periodicity should appear in a rotationally aligned MoS_2/WSe_2 bilayer; namely, the rotational angle between two atomic lattices is either 0° (R) or 180° (H) (*27*, *28*). A simulated Moiré supercell for 0° rotational angle is displayed in Fig. 1C, resembling the STM observation well. However, the STM is unable to resolve the R or H stacking because the chalcogen sublattice on the surface will look identical. We then use annular dark-field scanning transmission electron microscopy (ADF-STEM) to unravel the atomic structure that is consistent with an R stacking.

STEM samples are prepared by exfoliating the on-top TMD layers together with a very thin graphite layer. The ADF image intensity increases with the atomic number and the number of atomic layers. This makes the signal from ultrathin graphite much weaker than the signals from bilayer TMDs, which could be simply treated as background signals. The ADF-STEM image of the heterostructure stack is shown in Fig. 1D. Although MoS_2 and WSe_2 are rotationally aligned, their difference in lattice constants leads to locally different lateral registries, resulting in a periodic variation of these local alignments (that is, the Moiré pattern). In Fig. 1E, we show the ADF-STEM images at different local alignments [designated as AA, AB_{Se}, Bridge (Br), and AB_W] along with the simulated ADF-STEM images, which fit well with the experimental ones, and the corresponding models on the left. The symbol of

[1]Department of Physics, University of Texas at Austin, Austin, TX 78712, USA. [2]Institute of Atomic and Molecular Sciences, Academia Sinica, P.O. Box 23-166, Taipei 10617, Taiwan. [3]State Key Laboratory of Silicon Materials and School of Materials Science and Engineering, Zhejiang University, Hangzhou, Zhejiang 310027, People's Republic of China. [4]Physical Science and Engineering Division, King Abdullah University of Science and Technology, Thuwal 23955-6900, Kingdom of Saudi Arabia. [5]Research Center for Applied Sciences, Academia Sinica, Taipei 10617, Taiwan. [6]School of Physics, Georgia Institute of Technology, Atlanta, GA 30332, USA. [7]Department of Physics, National Taiwan University, Taipei 10617, Taiwan.
*Corresponding author. Email: shih@physics.utexas.edu

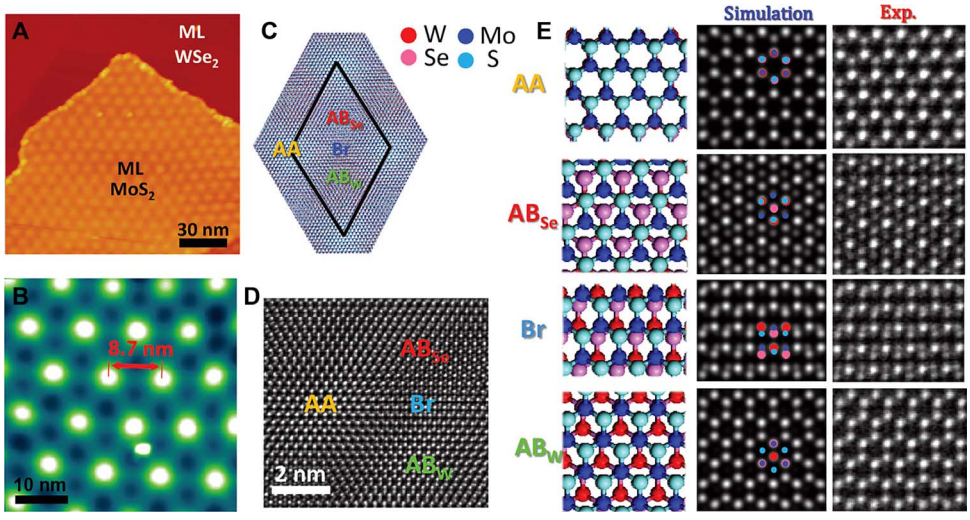

Fig. 1. Atomic structure of as-grown MoS_2/WSe_2 vdW heterostructures revealed by STM and STEM. (**A**) STM image for a MoS_2/WSe_2 vdW heterostructure on the highly oriented pyrolytic-graphite (HOPG) substrate. (**B**) Close-up STM image showing the hexagonal Moiré pattern with a periodicity of 8.7 nm. (**C**) Schematic model of the Moiré pattern on an R-stacked MoS_2/WSe_2 hetero-bilayer. By using the lattice constants of 3.16 Å for MoS_2 and 3.28 Å for WSe_2, the simulated supercell marked by black solid lines shows a periodicity of 8.64 nm. (**D**) Atomically resolved STEM image. Typical regions in an R-stacked heterostructure—AA, AB_{Se}, Br, and AB_W—are labeled in both (C) and (D). The close-up STEM images for each region are shown in the right column of (**E**). The simulated images (based on an R-type stacking) and their corresponding atomic models are displayed in the middle and left columns of (E), respectively. (A and B) −3.0 V, 10 pA. Exp., experimental.

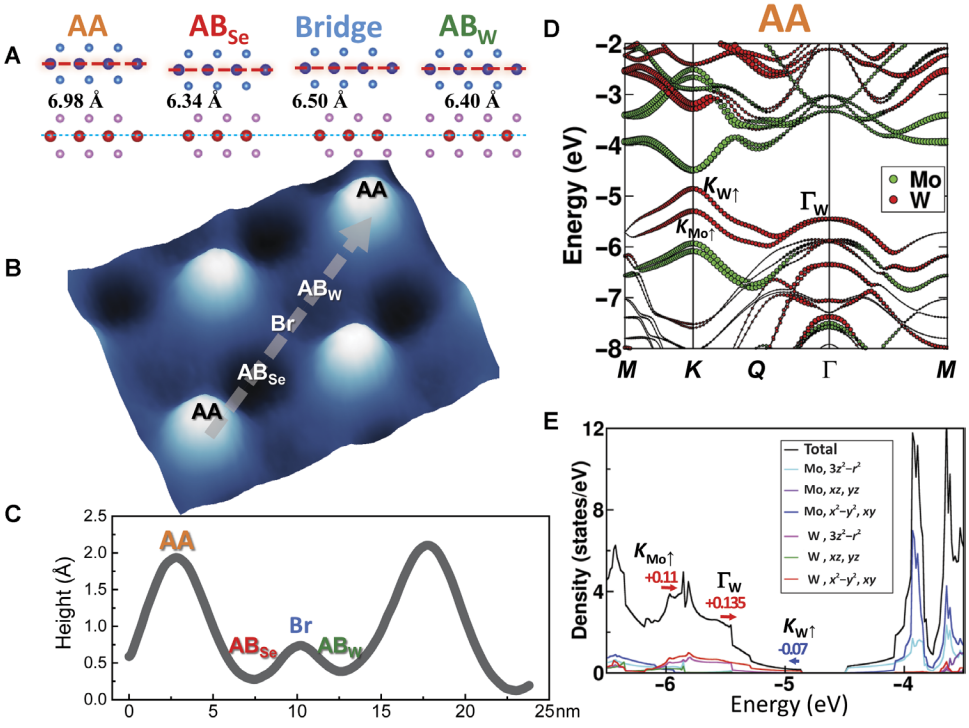

Fig. 2. First-principles calculations for the interlayer separations and electronic structures of representative sites in an R-stacked MoS_2/WSe_2 heterostructure. (**A**) Side views of the atomic models for AA, AB_{Se}, Br, and AB_W regions with an average lattice constant (Supplementary Materials). The calculated interlayer separations for four atomic alignments are labeled in (A). (**B**) A perspective view of an STM image zoomed in on a unit cell of the Moiré pattern. A height profile along the diagonal line from AA to AA [gray dashed line in (B)] is shown in (**C**). Energy band structure of the AA registry is displayed in (**D**), whereas its corresponding density of states (DOS) diagrams are shown in (**E**). The size of the green (red) circles represents the projected weight on the *d* orbitals of Mo (W), and the states are labeled in the subscript based on this project. The corrections for the strain resulting from the average lattice constant used in the calculation are labeled for the typical critical points in the DOS diagram. Results for other sites can be found in the Supplementary Materials. (B) −3.0 V, 10 pA.

AB_{Se} (AB_W) means that the hexagonal lattices of the metal atoms in the two MLs are stacked in an AB manner (analogous to bilayer graphene), with the Se(W) atoms in the bottom ML not covered by any atoms in the upper ML. A more detailed ADF-STEM analysis, including intensity line profile analysis in different regions, can be found in figs. S1 and S2.

The rotationally aligned MoS_2/WSe_2 stack has a lattice constant of 8.7 nm, and a unit cell contains about 4000 atoms. Theoretically, it is very challenging to use a very large unit cell for electronic structure calculations with density functional theory (DFT). To circumvent this difficulty, we first examine the effect of different local interlayer atomic registries on the electronic structure using the average lattice constant for both MoS_2 and WSe_2 (see the Supplementary Materials for details). It is expected that the results reflect the corresponding changes caused by the local registry in the large unit cell. The calculated band diagram for the AA site is shown in Fig. 2D (other sites are shown in fig. S3). The interlayer separations at different sites (labeled in Fig. 2A), which show an order of AA > Br > AB_W > AB_{Se}, are also calculated. These differences in height can be used to distinguish the high-symmetry sites in STM observations (detailed discussion in the Supplementary Materials). As shown in Fig. 2 (B and C), AA, AB_{Se}, Br, and AB_W are labeled along the diagonal line of one supercell, following the same sequence predicted by calculations despite a smaller amplitude in their differences.

The second step of the theoretical calculation entails a posterior strain correction to gain a more accurate description for the electronic structure of individual "unstrained" MLs. This is justifiable because little mixing exists between electronic states coming from different layers in the bilayer system. These strain corrections lead to systematic shifts in critical point energy locations, as labeled by the arrows shown in Fig. 2E. It is found that significant differences exist in electronic structures between AA and AB_{Se} sites, especially for electronic states at the Γ point in the valence band. This is due to the fact that the interlayer coupling at the Γ point is mediated through the chalcogen p_z orbitals. The difference in the local atomic registry (for example, AA versus AB_{Se}) is primarily in the lateral alignment of the chalcogen atoms, that is, Se in the top WSe_2 layer and S in the bottom MoS_2 layer, as shown in Fig. 2A. Consequently, interlayer coupling would be significantly influenced. Theoretical calculations for energy locations (after strain correction) of key critical points for these four different local atomic registries are shown in Fig. 3D. Not all of them are resolved experimentally. Up arrow

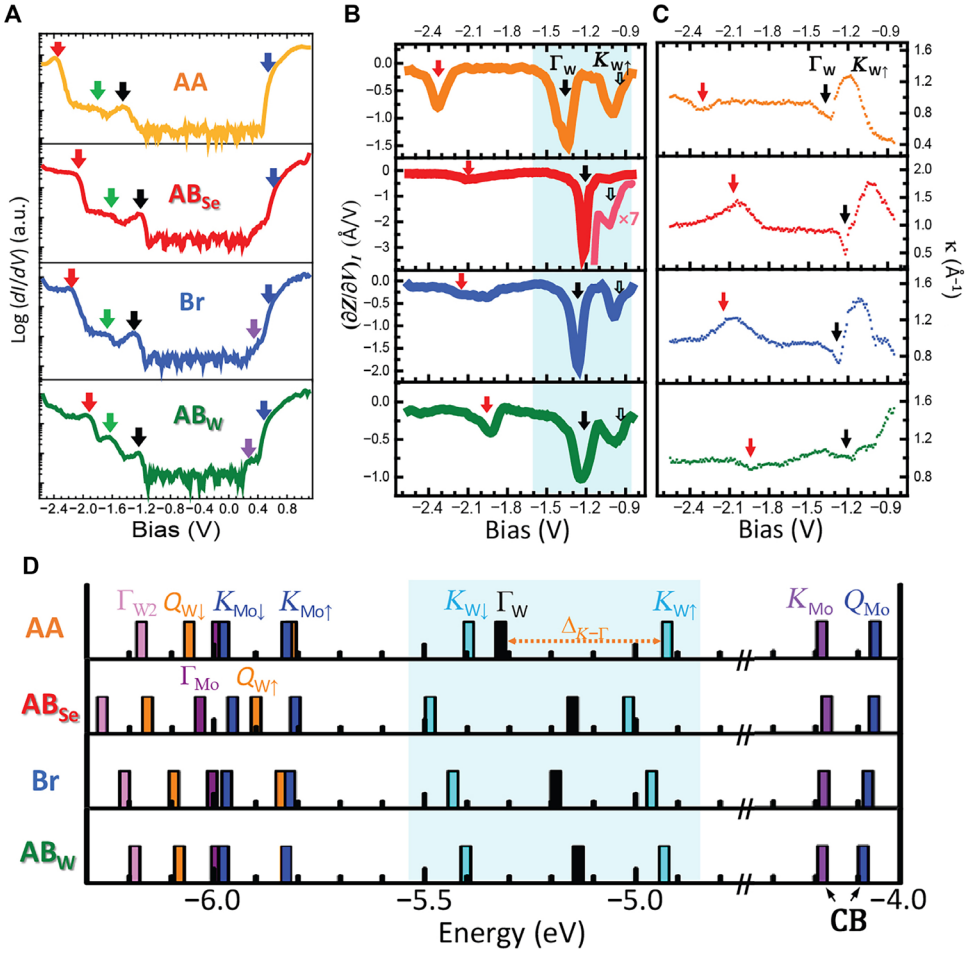

Fig. 3. Scanning tunneling spectra of AA, AB_{Se}, Br, and AB_W regions. (**A**) *dI*/*dV* spectra. (**B** and **C**) $(\partial Z/\partial V)_I$ and decay constant κ spectra of valence bands, respectively. (**D**) Calculated energy values at key critical points for AA, AB_{Se}, Br, and AB_W sites, respectively. The energies are with respect to the vacuum level. The shaded regions in (B) and (D) represent the valence band edges and show consistent movements of the energy locations of Γ_W (black) and K_W (cyan). In a deeper lying energy range, the spectral features marked by red and green arrows in (A) to (C) correspond to the energy window where the $Q_{W\uparrow,\downarrow}$, $K_{Mo\uparrow,\downarrow}$, and Γ_{Mo} states and a lower Γ_W (labeled as Γ_{W2}) state are located. The complicated movements in their relative energy locations result in a complex behavior in κ spectra [red arrows in (C)], making the direct identification of individual states nontrivial.

and down arrow subscripts are used to represent the higher and lower energy levels in spin-orbit split K (Q) states, respectively.

STM and STS reveal detailed information on how interlayer atomic registry affects the local electronic structures of the MoS_2/WSe_2 heterobilayer. In Fig. 3, three different STS modes are displayed: the conventional dI/dV acquired at constant Z (Fig. 3A), the $\partial Z/\partial V$ at constant current (Fig. 3B), and the tunneling decay constant defined as $\kappa = -1/2\ (d\ln I/dZ)$ (Fig. 3C). As discussed recently, the $(\partial Z/\partial V)_I$ spectrum provides the signature for the onset of different thresholds in the tunneling process, whereas the κ spectrum helps us to identify the origin of these thresholds in the Brillouin zones (*29*).

In the conventional dI/dV spectrum (displayed in the logarithmic scale), several spectral features are identified (labeled with arrows in different colors). The states marked by the black arrows are the Γ_W states that reside primarily in the WSe_2 layer (Fig. 2D). This assignment is corroborated by both the $(\partial Z/\partial V)_I$ and the κ measurements shown in Fig. 3 (B and C). At a constant current, when the sample bias (V_S) is scanned from below to above Γ_W, the loss of Γ_W states forces the tip to move inward to compensate for this loss, resulting in a dip in the $(\partial Z/\partial V)_I$ (that is, a sudden drop in Z). This allows us to probe a critical point in the band structure. Moreover, because the parallel momentum $k_{\|} = 0$ at the Γ point, one anticipates to observe a sharp minimum in κ, as $\kappa = \sqrt{\frac{2m\phi_o}{\hbar^2} + k_{\|}^2}$, where ϕ_o is the barrier height. This is observed in Fig. 3C (marked by black arrows).

In the dI/dV spectra acquired with Z stabilized at $V_S = -2.6$ V, the Z value is not small enough to detect the states above Γ_W (particularly states near $K_{W\uparrow}$) because of their high decay constant. In the constant current spectrum, this sensitivity issue is removed. The threshold at $K_{W\uparrow}$ appears as another dip in $(\partial Z/\partial V)_I$. This occurs when the sample bias is moved above the energy location of K_W, and the tip needs to move closer to the sample to achieve tunneling to the underlying graphite states. The large decay constant κ measured near $K_{W\uparrow}$ also reflects the high $k_{\|}$ value. It should be noted that because of the mixing of underlying graphite states in tunneling, simulation becomes necessary for an accurate determination of K_W, which suggests that the location of K_W is slightly above the dip location of $(\partial Z/\partial V)_I$ by about 0.05 eV (*29*).

The behavior of the electronic states near the valence band maximum (VBM) corroborated very well with the theoretical calculations shown in Fig. 3D, particularly for states near the VBM (shaded region in Fig. 3, B and D). These states (Γ_W and K_W) have spectral weights located at the WSe_2 layer. The theoretical results are in excellent agreement with the experimental result in energy locations of the Γ_W (showing an order of AA < Br < AB_{Se} < AB_W) and the energy separations between Γ_W and $K_{W\uparrow}$ (labeled as $\Delta_{K-\Gamma}$ and shown in Fig. 4A). The $K_{W\uparrow}$ state is located above Γ_W, and its signature can be identified much more clearly because it occurs in the bias range where Γ_W no longer contributes to the tunneling current. On the other hand, the state $K_{W\downarrow}$ is located below Γ_W, making its signature difficult to be detected because the tunneling current would be dominated by the states that originated near Γ_W. In a deeper lying energy range (marked by the red and green arrows in Fig. 3A), theory shows that these states correspond to the energy window where the Q_W, K_{Mo}, and Γ_{Mo} states and a lower Γ_W (labeled as Γ_{W2} in Fig. 3D) state are intertwined. The complicated movements in their relative energy locations make the direct identification of individual states nontrivial. Nevertheless, on the basis of the comparison with theoretical calculations (Fig. 3D), the features marked by the green arrows in Fig. 3A can be tentatively attributed to be $K_{Mo\uparrow}$ states.

In the conduction band, near the band edge, two clear thresholds (labeled with blue and purple arrows in Fig. 3A) are observed at the AB_{Se}, Br, and AB_W sites, similar to those observed in isolated ML-MoS_2 (*29*, *30*). These two thresholds have been previously identified as thresholds at two different critical points, Q and K, with the conduction band minimum (CBM) located at the K point. At the AA site, the lower threshold is not present because of a large tip-to-sample distance at the AA site for the stabilization voltage (−2.6 V) used in constant Z spectroscopy. The energy separation between these two thresholds remains relatively unchanged (~0.20 eV), but their absolute energy locations are site-dependent. The positions of the conduction band Q point follow the order of AA ~ AB_{Se} > Br > AB_W. The total change for the Q point position from AB_{Se} to AB_W is ~0.1 eV (similarly for the K point). Theoretical calculations show a similar order in the energy location (Fig. 3D), although the variation is smaller (only ~0.03 eV).

A very important consequence of interlayer coupling is that the local bandgap E_g is site-dependent. For example, at the AB_{Se} site, E_g = 1.30 eV with the VBM located at −0.98 eV and the CBM located at +0.32 eV. On the other hand, at the AB_W site, E_g = 1.14 eV with the VBM located at −0.93 eV and the CBM located at +0.21 eV. Experimental results for E_g at four different sites are shown in Fig. 4B, with the calculated E_g shown as brown circles. It is understood that DFT calculations significantly underestimate the bandgap values (*31*, *32*),

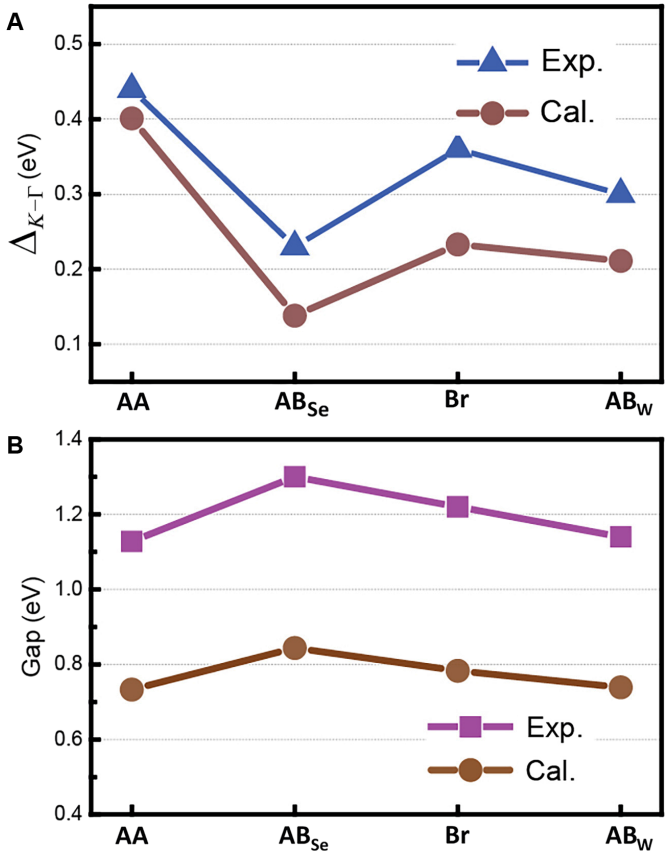

Fig. 4. Summary of the site-dependent electronic structures in MoS_2/WSe_2 heterobilayers. (**A**) Energy differences between K_W and Γ_W ($\Delta_{K-\Gamma}$) for the four different local lateral alignments. The experimental values are labeled as blue triangles, whereas the calculated DFT results are presented as brown circles. (**B**) Local bandgap E_g formed between the CBM of MoS_2 and the VBM of WSe_2. Experimental and calculated DFT results are displayed in purple and brown, respectively.

but the current results excellently replicate the overall trend in bandgap variations observed experimentally.

The periodic variation of local electronic structures as a consequence of the variation of the interlayer coupling due to the difference in local interlayer atomic registry of the MoS_2/WSe_2 hetero-bilayer also indicates the formation of an electronic superlattice. This is similar to the case of the graphene-hBN hetero-bilayer, except that the amplitude of bandgap variations is much larger in the current case. The formation of this electron superlattice is also visualized in the sequence of bias-dependent images shown in Fig. 5.

At a high negative bias, that is, from −3.0 to −2.4 V, a similar STM contrast is observed (Fig. 5, A and B). However, at −2.3 V, where the spectral feature of the AA site at −2.4 V (marked by the red arrow in Fig. 3A) is out of the tunneling range, a lowering of the topographic height at the AA site occurs. Accompanying this lowering is the appearance of three new features surrounding AA. These new features correspond to the locations of other bridge sites (labeled as Br_2 and discussed in more detail in the Supplementary Materials). Theory indicates that the electronic structures of Br_2 and Br are nearly the same. Indeed, at above −2.1 V, Br_2 and Br features merge, forming a circular ring feature. At −1.6 V, Γ_W states at all four sites are still in the tunneling window, and the AA site remains to have the highest topographic height. The most marked change is the turning of the bright feature at the AA site into a deep hole at −1.4 V. This is due to the fact that the Γ_W state at the AA site moves out of the tunneling window, whereas that of the other sites continues to contribute. The evolution continues as states at different sites move out of the tunneling window at a slightly different bias (discussed further in the Supplementary Materials). In the positive bias range, when the bias is above 0.85 V, all images have a "normal" contrast. At 0.5 V, the Q_{Mo} states at AA and AB_{Se} start to move out of the tunneling window, and the topographic height drops (note that the AB_{Se} site is the lowest in the first place and the drop does not lead to a contrast change as marked as that at the AA site). Because the AB_W site has the lowest CBM location (see Fig. 3A marked by the purple arrow), the AB_W site becomes the highest topographic feature as the bias continues to decrease to 0.2 V.

These rich features in the evolution of the bias-dependent STM images are just another manifestation of the lateral modulation of the electronic structures due to the local variation of interlayer atomic registry in the hetero-bilayer. The states that are affected the most are the valence states at the Γ point. However, the VBM of the overall double-layer stack remains at the *K* position, whose spectral weight is completely at the WSe_2 layer, whereas the CBM is also at the *K* position, but the spectral weight is completely at the MoS_2 layer. Thus, the notion of an interfacial exciton is unperturbed despite the fact that there is a strong enough interlayer coupling that changes other parts of the electronic structure significantly, but most importantly, the local bandgap of the double-layer stacks is modulated periodically with an amplitude of ~0.15 eV, forming a 2D electronic superlattice defined by the Moiré pattern. This would also mean that the interfacial exciton will experience a periodic potential modulation as large as 0.15 eV.

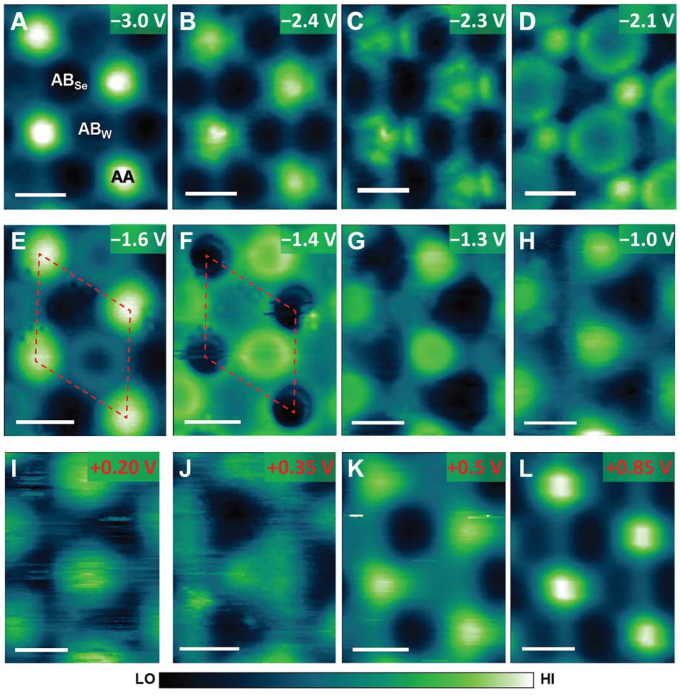

Fig. 5. Bias-dependent STM images of the Moiré pattern. The corresponding sample bias voltage is labeled for each image as shown. A dashed red rhombus in (**E**) and (**F**) represents a unit cell of the superlattice. A color bar is shown at the bottom to represent the relative height differences (that is, low and high) in (**A**) to (**L**). Scale bars, 5 nm in all images.

CONCLUSION

Our study clearly shows that the atomic registry between vdW layers dictates the behavior of interlayer electronic coupling, which can be used as a designing parameter for novel 2D electronic systems based on vdW heterostructures. The same principle should be commonly applicable to twisted vdW hetero-bilayers as well. The large amplitude of bandgap modulation raises the prospects for device applications at room temperature for these 2D electronic superlattices. Our findings will stimulate research interests in similar superstructures extensively formed in the flourishing family of 2D materials (*33*–*37*).

MATERIALS AND METHODS

Growth of MoS_2/WSe_2 vdW heterostructure samples

The WSe_2/MoS_2 vdW heterostructures were grown using the developed two-step CVD method (*26*, *38*). First, an ML WSe_2 single crystal was grown on the HOPG substrate. The WO_3 powder (0.6 g) was placed in a quartz boat located in the heating zone center, and the HOPG substrate was put at the downstream side. The Se powder was placed in a separate quartz boat at the upper stream side of the quartz tube. The Se powder was heated to 260°C and brought to the downstream side by an Ar/H_2 flow [Ar = 90 standard cubic centimeters per minute (sccm) and H_2 = 6 sccm], and the chamber pressure was controlled at 20 torr. The WO_3 powder was heated to 935°C for growth. After reaching the desired growth temperature, it was kept for 15 min, and the furnace was then naturally cooled down to room temperature. The as-grown WSe_2 sample was then put into a separate furnace for the second step of MoS_2 growth. The setup for MoS_2 synthesis is similar to that for WSe_2, and the reactants were changed to MoO_3 (0.6 g) and S. The Ar gas flow was set at 70 sccm, and the pressure was controlled at 40 torr. The MoO_3 and S sources were heated to 755° and 190°C, held for 15 min for synthesis, and then naturally cooled down to room temperature.

STM and STS

STM and STS investigations were acquired at 77 K in ultrahigh vacuum (base pressure, $<6 \times 10^{-11}$ torr). Electrochemically etched W-tips were cleaned in situ with electron beam bombardment. The tunneling bias was applied to the sample. The dI/dV spectroscopy at constant Z was taken by using a lock-in amplifier with a modulation voltage of 10 mV at a frequency of 914 Hz. The $(\partial Z/\partial V)_I$ spectra were acquired by sweeping the sample bias while feedback loop was on (constant tunneling current). The tunneling decay constant κ is equal to $-d\ln I/2dZ \equiv -(dI/dZ)/2I_0$. dI/dZ can be acquired by using the lock-in amplifier with a Z-modulation amplitude of 0.01 nm and a modulation frequency of 914 Hz, which is faster than the feedback time constant. This results in a small current modulation superimposed on the feedback set current I_0. If the sample bias is swept slowly, the κ and $(\partial Z/\partial V)_I$ can be acquired at the same time.

ADF-STEM characterization and image simulation

The sample was transferred onto a TEM grid following a previous report with minor modifications (*39*). ADF-STEM images were recorded with a probe-corrected Titan ChemiSTEM (FEI), which was operated at an acceleration voltage of 200 kV. The probe current was set at 47 pA with a convergent angle of 22 mrad for illumination. The inner collection angle was adjusted to 44 mrad to enhance the contrast of sulfur atoms. The experimental ADF-STEM images shown in the main text were superimposed by 10 frames after drift compensation and then processed with an improved Wiener filtering method to increase the signal-to-noise ratio for a better display. ADF-STEM image simulations were performed using QSTEM software (*40*), with the input parameters being the same as the experimental settings.

First-principles calculations

First-principles calculations were carried out using DFT as implemented in the Vienna Ab initio Simulation Package (*41*). The interaction between electrons and ionic cores was approximated by the projector augmented wave method (*42*), and the exchange-correlation potential was described by the Perdew-Burke-Ernzerhof generalized gradient approximation (*43*), with the vdW correction incorporated by the vdW-DF (optB86) functionals (*44*). A supercell size of 25 Å along the z direction was used with a vacuum thickness larger than 18 Å to eliminate the spurious interaction in the slab calculation, and the energy cutoff of plane waves was 600 eV. The structure was fully relaxed until the change of the energy and the force reached 10^{-6} eV per 1×1 cell and 10^{-3} eV/Å, respectively. A $12 \times 12 \times 1$ k-grid was used for 1×1 unit cell of MoS_2/WSe_2, and a finer k-grid of $81 \times 81 \times 1$ was used for the DOS calculation with the spin-orbit coupling effect included for both the DOS and electronic band structure calculations. To perform calculations for the local atomic alignments, we used an average lattice constant of 3.23 Å for both MoS_2 and WSe_2 to create the 1×1 unit cell. The strain effects resulting from the usage of the averaged lattice parameter were estimated by comparing the band structures of unstrained and strained (3.23 Å) freestanding MLs (details in the Supplementary Materials). These strain effects were corrected in Figs. 3D and 4.

SUPPLEMENTARY MATERIALS

Supplementary material for this article is available at http://advances.sciencemag.org/cgi/content/full/3/1/e1601459/DC1

Determining the R stacking and local atomic registries by intensity profiles of STEM images
First-principles calculation of the site-dependent band structures
Additional discussions for STM and STS results
fig. S1. ADF-STEM results of the MoS_2/WSe_2 heterostructures.
fig. S2. Intensity profile along AA-to-AB_W in STEM images.
fig. S3. First-principles calculations of the electronic structures of AB_{Se}, Br, and AB_W.
fig. S4. Atomic model and the electronic structures of the Br_2 site.
fig. S5. Statistical distributions of the Γ_W energy locations.
table S1. Calculation results of the energy differences between key critical points.

REFERENCES AND NOTES

1. A. K. Geim, I. V. Grigorieva, Van der Waals heterostructures. *Nature* **499**, 419–425 (2013).
2. B. Hunt, J. D. Sanchez-Yamagishi, A. F. Young, M. Yankowitz, B. J. LeRoy, K. Watanabe, T. Taniguchi, P. Moon, M. Koshino, P. Jarillo-Herrero, R. C. Ashoori, Massive Dirac fermions and hofstadter butterfly in a van der Waals heterostructure. *Science* **340**, 1427–1430 (2013).
3. M. Yankowitz, J. Xue, D. Cormode, J. D. Sanchez-Yamagishi, K. Watanabe, T. Taniguchi, P. Jarillo-Herrero, P. Jacquod, B. J. LeRoy, Emergence of superlattice Dirac points in graphene on hexagonal boron nitride. *Nat. Phys.* **8**, 382–386 (2012).
4. C. R. Woods, L. Britnell, A. Eckmann, R. S. Ma, J. C. Lu, H. M. Guo, X. Lin, G. L. Yu, Y. Cao, R. V. Gorbachev, A. V. Kretinin, J. Park, L. A. Ponomarenko, M. I. Katsnelson, Y. N. Gornostyrev, K. Watanabe, T. Taniguchi, C. Casiraghi, H.-J. Gao, A. K. Geim, K. S. Novoselov, Commensurate-incommensurate transition in graphene on hexagonal boron nitride. *Nat. Phys.* **10**, 451–456 (2014).
5. J. Xue, J. Sanchez-Yamagishi, D. Bulmash, P. Jacquod, A. Deshpande, K. Watanabe, T. Taniguchi, P. Jarillo-Herrero, B. J. LeRoy, Scanning tunnelling microscopy and spectroscopy of ultra-flat graphene on hexagonal boron nitride. *Nat. Mater.* **10**, 282–285 (2011).
6. C. R. Dean, L. Wang, P. Maher, C. Forsythe, F. Ghahari, Y. Gao, J. Katoch, M. Ishigami, P. Moon, M. Koshino, T. Taniguchi, K. Watanabe, K. L. Shepard, J. Hone, P. Kim, Hofstadter's butterfly and the fractal quantum Hall effect in moire superlattices. *Nature* **497**, 598–602 (2013).
7. L. A. Ponomarenko, R. V. Gorbachev, G. L. Yu, D. C. Elias, R. Jalil, A. A. Patel, A. Mishchenko, A. S. Mayorov, C. R. Woods, J. R. Wallbank, M. Mucha-Kruczynski, B. A. Piot, M. Potemski, I. V. Grigorieva, K. S. Novoselov, F. Guinea, V. I. Fal'ko, A. K. Geim, Cloning of Dirac fermions in graphene superlattices. *Nature* **497**, 594–597 (2013).
8. J. Jung, A. M. DaSilva, A. H. MacDonald, S. Adam, Origin of band gaps in graphene on hexagonal boron nitride. *Nat. Commun.* **6**, 6308 (2015).
9. P. Rivera, K. L. Seyler, H. Yu, J. R. Schaibley, J. Yan, D. G. Mandrus, W. Yao, X. Xu, Valley-polarized exciton dynamics in a 2D semiconductor heterostructure. *Science* **351**, 688–691 (2016).
10. H. Yu, Y. Wang, Q. Tong, X. Xu, W. Yao, Anomalous light cones and valley optical selection rules of interlayer excitons in twisted heterobilayers. *Phys. Rev. Lett.* **115**, 187002 (2015).
11. P. Rivera, J. R. Schaibley, A. M. Jones, J. S. Ross, S. Wu, G. Aivazian, P. Klement, K. Seyler, G. Clark, N. J. Ghimire, J. Yan, D. G. Mandrus, W. Yao, X. Xu, Observation of long-lived interlayer excitons in monolayer $MoSe_2$–WSe_2 heterostructures. *Nat. Commun.* **6**, 6242 (2015).
12. X. P. Hong, J. Kim, S. F. Shi, Y. Zhang, C. H. Jin, Y. Sun, S. Tongay, J. Wu, Y. Zhang, F. Wang, Ultrafast charge transfer in atomically thin MoS_2/WS_2 heterostructures. *Nat. Nanotechnol.* **9**, 682–686 (2014).
13. K. F. Mak, C. Lee, J. Hone, J. Shan, T. F. Heinz, Atomically thin MoS_2: A new direct-gap semiconductor. *Phys. Rev. Lett.* **105**, 136805 (2010).
14. Y. Zhang, T.-R. Chang, B. Zhou, Y.-T. Cui, H. Yan, Z. Liu, F. Schmitt, J. Lee, R. Moore, Y. Chen, H. Lin, H. T. Jeng, S. K. Mo, Z. Hussain, A. Bansil, Z. X. Shen, Direct observation of the transition from indirect to direct bandgap in atomically thin epitaxial $MoSe_2$. *Nat. Nanotechnol.* **9**, 111–115 (2014).
15. A. J. Bradley, M. M. Ugeda, F. H. da Jornada, D. Y. Qiu, W. Ruan, Y. Zhang, S. Wickenburg, A. Riss, J. Lu, S.-K. Mo, Z. Hussain, Z.-X. Shen, S. G. Louie, M. F. Crommie, Probing the role of interlayer coupling and coulomb interactions on electronic structure in few-layer $mose_2$ nanostructures. *Nano Lett.* **15**, 2594–2599 (2015).
16. W. Jin, P.-C. Yeh, N. Zaki, D. Zhang, J. T. Sadowski, A. Al-Mahboob, A. M. van der Zande, D. A. Chenet, J. I. Dadap, I. P. Herman, P. Sutter, J. Hone, R. M. Osgood Jr., Direct measurement of the thickness-dependent electronic band structure of MoS_2 using angle-resolved photoemission spectroscopy. *Phys. Rev. Lett.* **111**, 106801 (2013).
17. A. M. van der Zande, J. Kunstmann, A. Chernikov, D. A. Chenet, Y. You, X. Zhang, P. Y. Huang, T. C. Berkelbach, L. Wang, F. Zhang, M. S. Hybertsen, D. A. Muller, D. R. Reichman, T. F. Heinz, J. C. Hone, Tailoring the electronic structure in bilayer molybdenum disulfide via interlayer twist. *Nano Lett.* **14**, 3869–3875 (2014).
18. P.-C. Yeh, W. Jin, N. Zaki, J. Kunstmann, D. Chenet, G. Arefe, J. T. Sadowski, J. I. Dadap, P. Sutter, J. Hone, R. M. Osgood Jr., Direct measurement of the tunable electronic structure of bilayer MoS_2 by interlayer twist. *Nano Lett.* **16**, 953–959 (2016).

19. S. Huang, X. Ling, L. Liang, J. Kong, H. Terrones, V. Meunier, M. S. Dresselhaus, Probing the interlayer coupling of twisted bilayer MoS_2 using photoluminescence spectroscopy. *Nano Lett.* **14**, 5500–5508 (2014).
20. A. A. Puretzky, L. Liang, X. Li, K. Xiao, B. G. Sumpter, V. Meunier, D. B. Geohegan, Twisted $MoSe_2$ bilayers with variable local stacking and interlayer coupling revealed by low-frequency raman spectroscopy. *ACS Nano* **10**, 2736–2744 (2016).
21. S. Tongay, W. Fan, J. Kang, J. Park, U. Koldemir, J. Suh, D. S. Narang, K. Liu, J. Ji, J. Li, R. Sinclair, J. Wu, Tuning interlayer coupling in large-area heterostructures with CVD-grown MoS_2 and WS_2 monolayers. *Nano Lett.* **14**, 3185–3190 (2014).
22. J. Zhang, J. Wang, P. Chen, Y. Sun, S. Wu, Z. Jia, X. Lu, H. Yu, W. Chen, J. Zhu, G. Xie, R. Yang, D. Shi, X. Xu, J. Xiang, K. Liu, G. Zhang, Observation of strong interlayer coupling in MoS_2/WS_2 heterostructures. *Adv. Mater.* **28**, 1950–1956 (2016).
23. M.-H. Chiu, C. Zhang, H.-W. Shiu, C.-P. Chuu, C.-H. Chen, C.-Y. S. Chang, C.-H. Chen, M.-Y. Chou, C.-K. Shih, L.-J. Li, Determination of band alignment in the single-layer MoS_2/WSe_2 heterojunction. *Nat. Commun.* **6**, 7666 (2015).
24. Y.-H. Zhao, F. Yang, J. Wang, H. Guo, W. Ji, Continuously tunable electronic structure of transition metal dichalcogenides superlattices. *Sci. Rep.* **5**, 8356 (2015).
25. H. Terrones, F. López-Urías, M. Terrones, Novel hetero-layered materials with tunable direct band gaps by sandwiching different metal disulfides and diselenides. *Sci. Rep.* **3**, 1549 (2013).
26. Y.-C. Lin, R. K. Ghosh, R. Addou, N. Lu, S. M. Eichfeld, H. Zhu, M.-Y. Li, X. Peng, M. J. Kim, L.-J. Li, R. M. Wallace, S. Datta, J. A. Robinson, Atomically thin resonant tunnel diodes built from synthetic van der Waals heterostructures. *Nat. Commun.* **6**, 7311 (2015).
27. I. Amidror, *The Theory of the Moiré Phenomenon* (Springer-Verlag, 2009).
28. G. Oster, M. Wasserman, C. Zwerling, Theoretical interpretation of moiré patterns. *J. Opt. Soc. Am.* **54**, 169–175 (1964).
29. C. Zhang, Y. Chen, A. Johnson, M.-Y. Li, L.-J. Li, P. C. Mende, R. M. Feenstra, C.-K. Shih, Probing critical point energies of transition metal dichalcogenides: Surprising indirect gap of single layer WSe_2. *Nano Lett.* **15**, 6494–6500 (2015).
30. C. Zhang, A. Johnson, C.-L. Hsu, L.-J. Li, C.-K. Shih, Direct imaging of band profile in single layer MoS_2 on graphite: Quasiparticle energy gap, metallic edge states, and edge band bending. *Nano Lett.* **14**, 2443–2447 (2014).
31. D. Y. Qiu, F. H. da Jornada, S. G. Louie, Optical spectrum of MoS_2: Many-body effects and diversity of exciton states. *Phys. Rev. Lett.* **111**, 216805 (2013).
32. H. Shi, H. Pan, Y.-W. Zhang, B. I. Yakobson, Quasiparticle band structures and optical properties of strained monolayer MoS_2 and WS_2. *Phys. Rev. B* **87**, 155304 (2013).
33. Y. Zhao, J. Qiao, P. Yu, Z. Hu, Z. Lin, S. P. Lau, Z. Liu, W. Ji, Y. Chai, Extraordinarily strong interlayer interaction in 2D layered PtS_2. *Adv. Mater.* **28**, 2399–2407 (2016).
34. J. Qiao, X. Kong, Z.-X. Hu, F. Yang, W. Ji, High-mobility transport anisotropy and linear dichroism in few-layer black phosphorus. *Nat. Commun.* **5**, 4475 (2014).
35. Z.-X. Hu, X. Kong, J. Qiao, B. Normand, W. Ji, Interlayer electronic hybridization leads to exceptional thickness-dependent vibrational properties in few-layer black phosphorus. *Nanoscale* **8**, 2740–2750 (2016).
36. J. Dai, X. C. Zeng, Bilayer phosphorene: Effect of stacking order on bandgap and its potential applications in thin-film solar cells. *J. Phys. Chem. Lett.* **5**, 1289–1293 (2014).
37. D. Çakır, C. Sevik, F. M. Peeters, Significant effect of stacking on the electronic and optical properties of few-layer black phosphorus. *Phys. Rev. B* **92**, 165406 (2015).
38. M.-Y. Li, Y. Shi, C.-C. Cheng, L.-S. Lu, Y.-C. Lin, H.-L. Tang, M.-L. Tsai, C.-W. Chu, K.-H. Wei, J.-H. He, W.-H. Chang, K. Suenaga, L.-J. Li, Epitaxial growth of a monolayer WSe_2-MoS_2 lateral p-n junction with an atomically sharp interface. *Science* **349**, 524–528 (2015).
39. C. T. Koch, thesis, Arizona State University (2002).
40. H. Liu, L. Jiao, F. Yang, Y. Cai, X. Wu, W. Ho, C. Gao, J. Jia, N. Wang, H. Fan, W. Yao, M. Xie, Dense network of one-dimensional midgap metallic modes in monolayer $MoSe_2$ and their spatial undulations. *Phys. Rev. Lett.* **113**, 066105 (2014).
41. G. Kresse, J. Furthmüller, Efficiency of ab-initio total energy calculations for metals and semiconductors using a plane-wave basis set. *Comput. Mater. Sci.* **6**, 15–50 (1996).
42. P. E. Blöchl, Projector augmented-wave method. *Phys. Rev. B* **50**, 17953–17979 (1994).
43. J. P. Perdew, K. Burke, M. Ernzerhof, Generalized gradient approximation made simple. *Phys. Rev. Lett.* **77**, 3865–3868 (1996).
44. J. Klimeš, D. R. Bowler, A. Michaelides, Van der Waals density functionals applied to solids. *Phys. Rev. B* **83**, 195131 (2011).

Acknowledgments: We thank F. Chan for his help on the sample transfer process and F. Lin for providing the improved Wiener filter. **Funding:** This research was supported by grants from the Welch Foundation (F-1672) and the U.S. NSF (DMR-1306878 and EFMA-1542747). L.-J.L. thanks the support from the King Abdullah University of Science and Technology (Saudi Arabia); the Ministry of Science and Technology and Taiwan Consortium of Emergent Crystalline Materials, Academia Sinica (Taiwan); and the Asian Office of Aerospace Research and Development (FA23861510001) (USA). The STEM work was financially supported by the National Basic Research Program of China (grant nos. 2015CB921004 and 2014CB932500) and the National Science Foundation of China (grant nos. 51472215 and 51222202). The STEM experiments used the resources in the Center of Electron Microscopy of Zhejiang University. C.-P.C. and M.-Y.C. acknowledge support from the Thematic Project at Academia Sinica and the U.S. NSF (EFMA-1542747). **Author contributions:** C.Z. carried out the STM and STS measurements. C.-P.C. and M.-Y.C. carried out the first-principles calculation. X.R. and C.J. performed the STEM investigations. M.-Y.L. and L.-J.L. grew the vdW MoS_2/WSe_2 heterostructures by CVD. C.-K.S. advised on the experiment and provided input on the data analysis. C.-K.S. and C.Z. wrote the paper with input from other coauthors. **Competing interests:** The authors declare that they have no competing interests. **Data and materials availability:** All data needed to evaluate the conclusions in the paper are present in the paper and/or the Supplementary Materials. Additional data related to this paper may be requested from the authors.

Submitted 27 June 2016
Accepted 28 November 2016
Published 6 January 2017
10.1126/sciadv.1601459

Citation: C. Zhang, C.-P. Chuu, X. Ren, M.-Y. Li, L.-J. Li, C. Jin, M.-Y. Chou, C.-K. Shih, Interlayer couplings, Moiré patterns, and 2D electronic superlattices in MoS_2/WSe_2 hetero-bilayers. *Sci. Adv.* **3**, e1601459 (2017).

Interlayer couplings, Moiré patterns, and 2D electronic superlattices in MoS_2/WSe_2 hetero-bilayers

Chendong Zhang, Chih-Piao Chuu, Xibiao Ren, Ming-Yang Li, Lain-Jong Li, Chuanhong Jin, Mei-Yin Chou and Chih-Kang Shih

Sci Adv **3** (1), e1601459.
DOI: 10.1126/sciadv.1601459